

Simulations of light distribution on new instrumented baffles surrounding Virgo end mirrors

A. Macquet¹, M. Andrés-Carcasona¹, M. Martínez^{1,2}, L.I.M. Mir¹, A. Romero-Rodríguez¹, and H. Yamamoto⁴

¹Institut de Física d'Altes Energies (IFAE), The Barcelona Institute of Science and Technology, Campus UAB, 08193 Bellaterra (Barcelona) Spain

²Institució Catalana de Recerca i Estudis Avancats (ICREA), Barcelona, Spain

⁴LIGO laboratory, California Institute of Technology (Caltech), Pasadena, CA, US

Abstract. As part of the second phase of Advanced Virgo upgrade program, instrumented baffles are being constructed to be installed around the end mirrors in the main arms, in continuation of what has been implemented for the input mode cleaner end mirror during phase I. These baffles will be equipped with photosensors, allowing for real-time monitoring of the stray light around the mirrors. In this paper, we present optical simulations of the light distribution in the detector's main cavities to assess the ability of the sensors to effectively monitor misalignment and defects on the mirrors' surface and to play a role in the pre-alignment of the interferometer.

1. Introduction

In its final configuration, Advanced Virgo Plus will be a dual-recycled Fabry-Perot-Michelson interferometer with a detection range between 150 – 260 Mpc for gravitational waves emitted by binary neutron stars mergers [1]. To achieve this level of sensitivity, two phases of upgrades are planned with several improvements intended to reduce the level of noise in the detector. The first phase is currently ongoing, and the second one will take place between the O4 and O5 observing runs, in 2024-2025.

As part of this upgrade program, new instrumented baffles will be installed around the end mirrors (EM) in the main arms, in order to provide an active monitoring of the distribution of scattered light at low angles. It is also planned to instrument the baffles surrounding the input mirrors (IM) after O5. A first instrumented baffle was installed in April 2021 around the EM of the input mode cleaner (IMC) to demonstrate this new technology. First measurements have been presented in Ref. [2], and are in good agreement with previous simulations of stray light in the IMC cavity [3]. The baffles in the main arms will be instrumented with 120 Si-based photodiodes provided by Hamamatsu photonics in Japan. They are similar to the ones installed on the IMC baffle [2, 4], based on the S13955-01 model. These sensors will have a dynamic range of 13 mW and a resolution of approximately 60 μ W. They will be read at a rate up to

1 kHz, allowing to correlate with interferometer glitches. The inner and outer radii of the baffle will be 26 cm and 40 cm, respectively, and the sensors will be arranged in five concentric rings at 27, 28, 29, 30, and 31 cm from the center of the EM. No sensor will be placed beyond 31 cm, because the field is shielded by a baffle located in the cryotrap at 5.4 m from the EM, which has an aperture of 60 cm. In the planned configuration, each ring will be populated by 24 photodiodes. The layout is shown in Figure 1, although the final design and total number of sensors may be subject to minor modifications due to technical constraints.

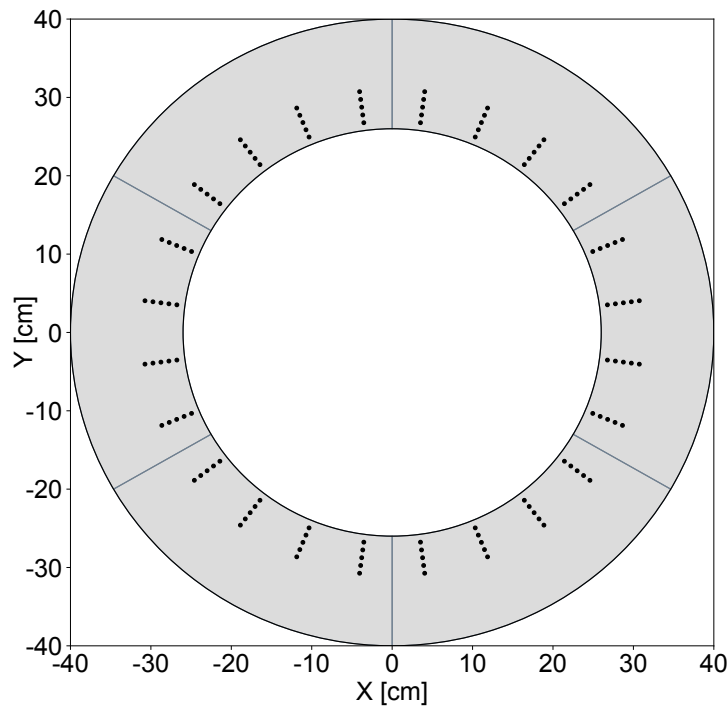


Figure 1. Planned layout of the sensors on the EM baffle.

In this paper, we assess the merits of these instrumented baffles using optical simulations of the light distribution in the main arms. First, we describe the simulation tool and the parameters used for this study. Then, we report the distribution of surface power on and around the main mirrors to estimate the amount of light that will be received by the baffles. We compute the power that will be seen by each sensor in different configurations, introducing misalignment and point defects on the mirrors, in order to assess the ability of the sensors to detect such defects.

2. Principle of the simulations

We use the *Stationary Interferometer Simulation*, SIS [5], to compute the fields in the main arms. SIS relies on fast Fourier transforms to calculate the propagation of the field in a realistic optical cavity, taking into account the roughness of mirrors, coating absorption and thermal deformations. The 2D distribution of the field can be extracted at any point of the cavity using an adaptative grid.

A sketch of the optical setup simulated is shown in Figure 2. It consists in a 3 km-long Fabry-Perot cavity that represents a Virgo main arm. To simulate the propagation of scattered light in the cavity, realistic maps of the mirrors' surface are used. For the IM, we use a surface map that has been measured during O3. Since the EM will be changed between O4 and O5, we do not have access to a measured surface map, so we use a simulated one [6]. In addition, the effect of the baffle that surrounds the cryotrap (often called cryobaffle) is taken into account by clipping the field at an aperture of 60 cm at this location. The clipped field is then allowed to propagate freely to the EM. Another cryobaffle is present in front of the IM, but it is not modelled in these simulations as its aperture is larger than the outer diameter of the IM baffle.

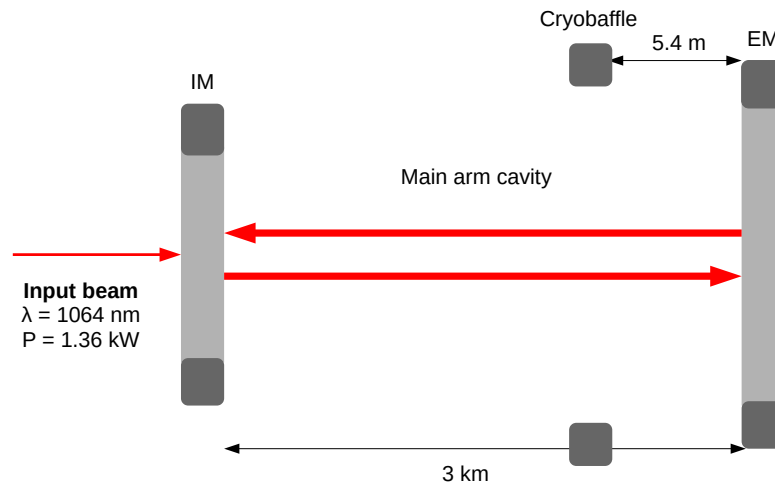


Figure 2. Sketch of the optical system simulated that represents a single Virgo arm. The power of the beam impinging on the IM is 1.36 kW, which corresponds to the expected value for O5 after the power recycling cavity. Baffles are represented in dark grey, and mirrors in light grey.

The main parameters used to perform the simulations are listed in Table 1. They correspond to the expected configuration of the detector during O5. The input power

is 1.36 kW and corresponds to the maximal expected power reaching the IM after the power-recycling cavity. The resolution of the grid over which the field is computed at the level of the EM is 0.64 mm.

Simulation parameters	
Input power	1.36 kW
Wavelength	1064 nm
EM aperture	52 cm
IM aperture	33 cm
EM transmittivity	$5 \cdot 10^{-6}$
IM transmittivity	$1.375 \cdot 10^{-2}$
EM RoC	1969 m
IM RoC	1067 m
EM thickness	20 cm
IM thickness	20 cm

Table 1. Parameters used to simulate Virgo main arms during O5.

We consider a layout of 5 rings of 24 sensors located at 27, 28, 29, 30, and 31 cm from the center of the EM, as displayed in Figure 1. We note $P(\phi, r)$ the power received by a sensor located at angle ϕ and distance r from the center of the mirror. This value is computed by integrating the surface power distribution over the area covered by the sensor. Since they will be placed behind conical holes of 4 mm of diameter, their effective area is 0.13 cm^2 . With a grid resolution of 0.64 mm, several pixels cover the area of one sensor. We can then compute the amount of power received by each sensor in different configurations, which will be shown at the end of next section.

3. Results

3.1. Nominal configuration

We define the nominal configuration as the case where the cavity is perfectly aligned, and realistic mirror maps are used. The distribution of surface power in the ensemble mirror plus baffle is shown in Figure 3 for the EM and IM. The effect of the cryobaffle is clearly visible on the EM with a sharp cut-off of the surface power at a radius of 30 cm.

The shape of the laser beam on the mirrors is represented in Figure 4, in the case where realistic mirror maps are used, and in the case where perfect mirrors are assumed. In the central region, the beams are almost perfectly Gaussian with a width of 9.1 cm and 4.9 cm on the EM and IM, respectively. These values are consistent with expectations for O5 [7]. The effect of mirror maps can be seen in the tails of the beam, which contain more power than with perfect mirrors. Thus, sensors located at radii between 27 and 31 cm are strategically placed to monitor scattered light.

Table 2 shows the total power circulating in the cavity and reaching the baffles. The total power circulating is 393 kW. This corresponds to the maximal expected power

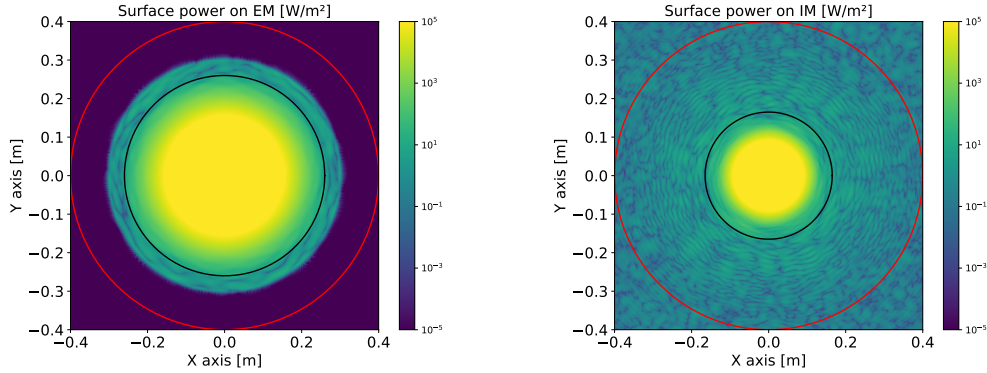


Figure 3. 2-D maps of the surface power distribution on the EM (left) and IM (right) in nominal configuration (perfectly aligned cavity and realistic mirror maps). The black and red circles indicate the inner and outer radius of the baffle, respectively.

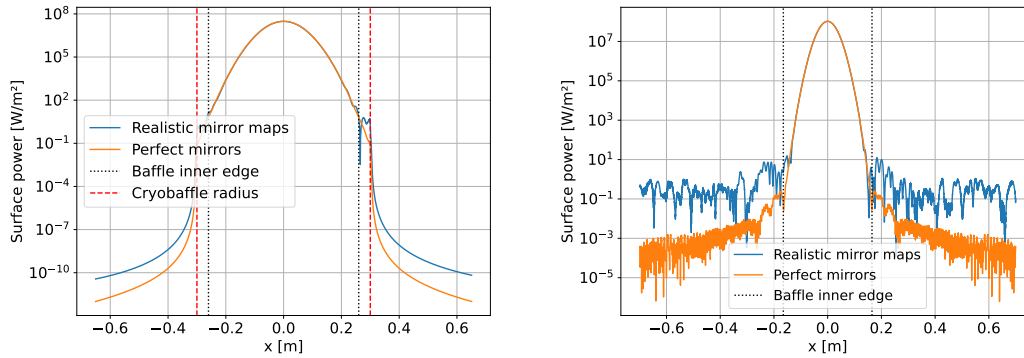


Figure 4. Distribution of power in EM (left) and IM (right) along the x axis in nominal configuration with realistic mirror maps (blue) and with perfect mirrors (orange). The black vertical lines indicate the baffle inner edge, and the red vertical lines in the left figure indicate the inner radius of the cryobaffle.

during O5 for a laser power of 130 W. The EM and IM baffles receive 0.22 W and 0.76 W, respectively, when realistic mirror maps are used, as compared to 0.10 W and 0.01 W when we consider perfect mirrors. For this reason, all the computations of the power received by sensors presented in the remainder of this paper are done with realistic mirror maps.

The amount of power reaching each sensor is shown in Figure 5. The average value is of the order of 10^{-4} W for the first four rings, and 10^{-9} W for the fifth ring at 31 cm from the center. This sharp drop is due to the cryobaffle that clips the field at a radius of 30 cm close to the EM. Because of the mirrors' roughness, the distribution of scattered light is not isotropic: in the innermost ring, the expected power in sensors varies between $5.62 \cdot 10^{-6}$ W and $4.69 \cdot 10^{-5}$ W, with a standard deviation of $1.18 \cdot 10^{-5}$ W. Since the resolution of the sensors is $6 \cdot 10^{-5}$ W, it is unlikely that these angular variations will be detected.

Simulation output	
Cavity power	393 kW
Power in EM baffle	$2.2 \cdot 10^{-1}$ W (0.6 ppm)
Power in IM baffle	$7.6 \cdot 10^{-1}$ W (1.9 ppm)
Beam width on EM	9.1 cm
Beam width on IM	4.9 cm

Table 2. Output of the simulation for the nominal configuration and realistic mirrors considered.

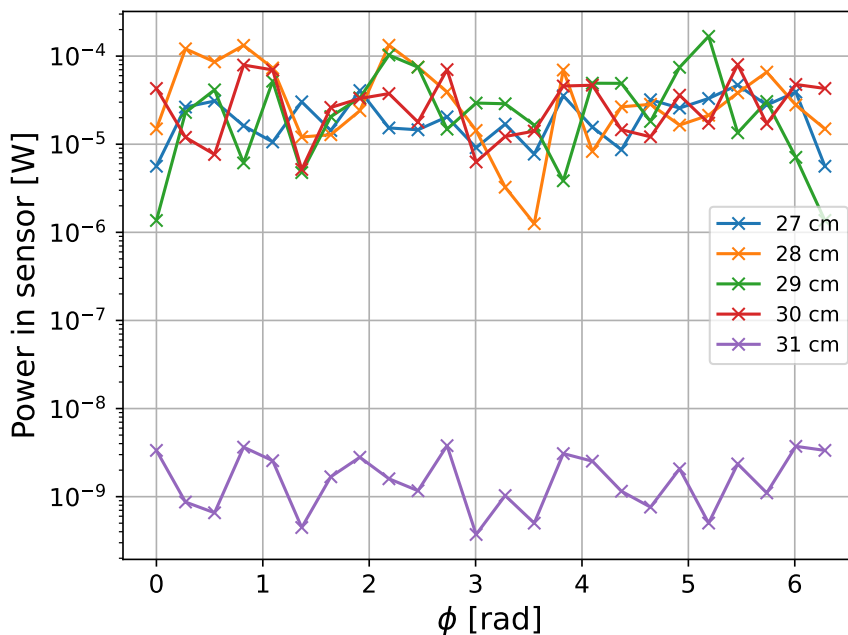


Figure 5. Power seen by each sensor in nominal configuration. Values are displayed for each ring as a function of the radial angle ϕ .

3.2. Misaligned cavity

Spurious misalignment of the interferometer's optics can induce the development of higher order modes in the laser beam and decrease the power circulating in the cavity, leading to an overall loss of sensitivity for the detector [8]. One of the main interests of instrumented baffles is to be able to detect such a misalignment. We simulate a misaligned cavity by introducing a tilt angle in the EM's surface map. This is equivalent to tilting the laser beam by the same angle in the opposite direction. As shown in Figure 6, the total power circulating in the cavity decreases as the tilt angle increases. The critical range for this value is between 10^{-7} rad, where the power starts to decrease by a few percents, to 10^{-6} rad, where the total power has decreased so much that the cavity becomes out of resonance. At $6.1 \cdot 10^{-7}$ rad, 50% of the power is lost.

We illustrate both regimes in Figure 7 by computing the amount of power seen by

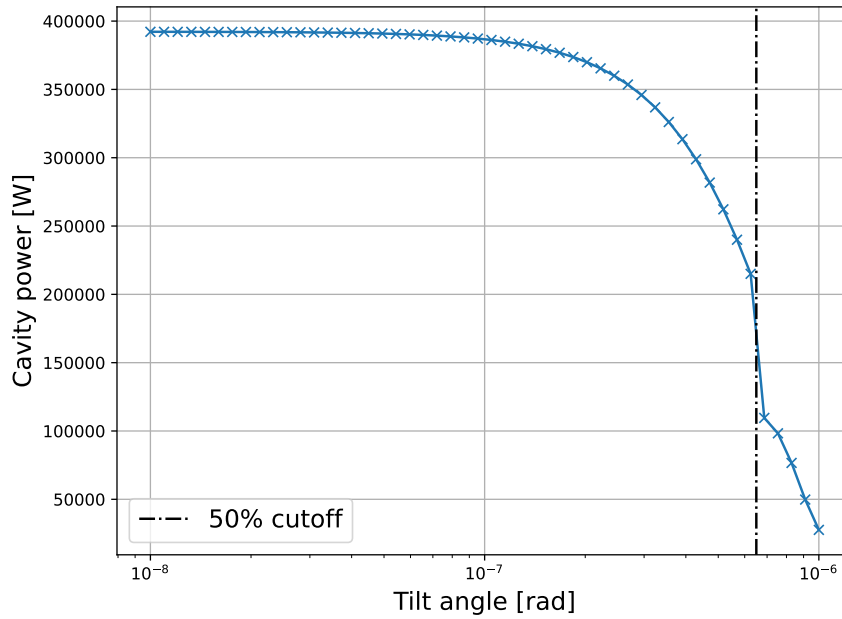


Figure 6. Total power circulating in the cavity as a function of the tilt angle applied to the EM.

each sensor for a tilt angle of $3 \cdot 10^{-7}$ rad, where the total power is around 90% of the value expected for a perfectly aligned cavity, and for an angle of $8 \cdot 10^{-7}$ rad, for which this value drops to 25%.

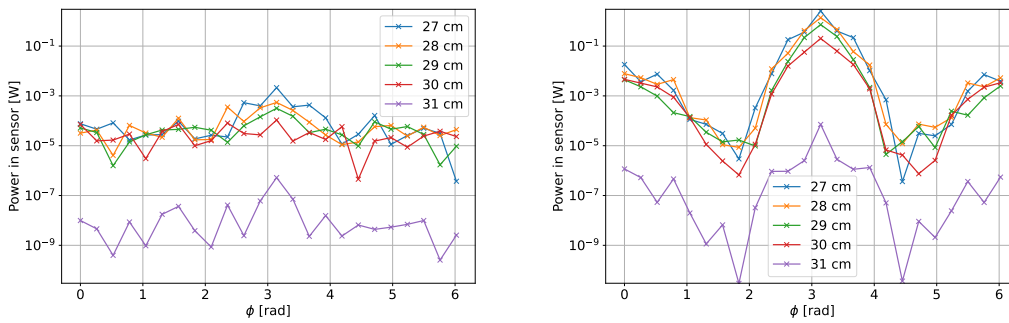


Figure 7. Power seen by each sensor when the EM is tilted by $3 \cdot 10^{-7}$ rad (left), and $8 \cdot 10^{-7}$ rad (right) along the x direction.

Since the beam does not hit the center of the mirror, an excess of power is seen in the sensors located around $\phi = \pi$, the direction of misalignment. Sensors located at lower radius receive more power. In the $3 \cdot 10^{-7}$ rad case, a sensor at 27 cm from the center of the mirror would see at most 2.1 mW of power, around 50 times more than in the nominal configuration. Therefore, such misalignment would be detectable by the sensors. When the tilt angle is $8 \cdot 10^{-7}$ rad, higher order modes of the beam start to

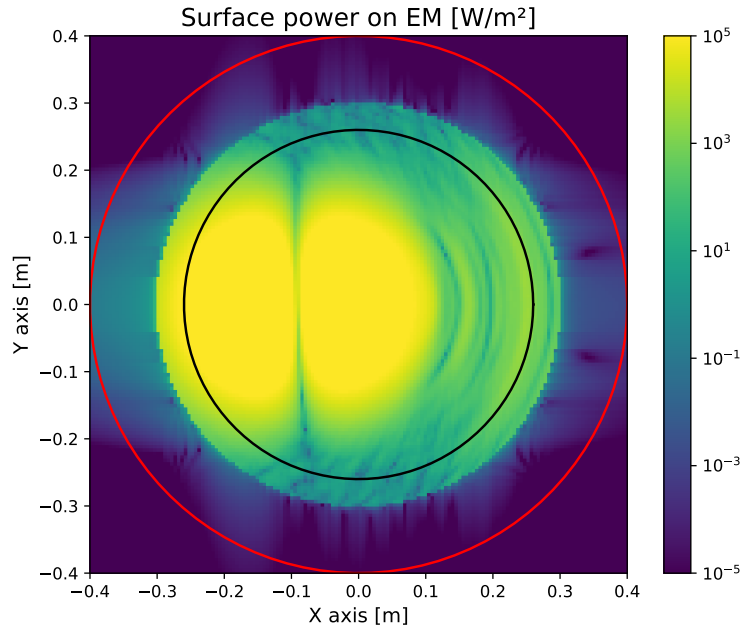


Figure 8. Surface power distribution on the EM when it is tilted by $8 \cdot 10^{-7}$ rad (right) along the x direction.

develop. In this case, the Hermite Gaussian mode $(1,0)$ is excited, as can be seen in Fig. 8. This explains the two dips around $\pi/2$ and $3\pi/2$ in the right panel of Fig. 7. Besides, sensors located in the first four rings would receive more than 1 W of power, which would almost certainly lead them to saturate. In this case of a large misalignment, sensors located in the fourth and fifth rings could continue to provide information after sensors from the inner rings saturate. As the tilt angle increases, sensors located in the direction of misalignment receive a higher fraction of the total power. However, the cavity power decreases quickly, as shown in Fig. 6. We find that the value of $8 \cdot 10^{-7}$ rad corresponds to the maximum power a sensor would see in the case of a misaligned cavity.

To show quantitatively how the sensors could be used to monitor misalignment, we define the differential power

$$\Delta P(\phi, r) = P(\phi, r) - P(\phi + \pi, r), \quad (1)$$

that is the difference of power in opposite sensors on the baffle. In the case of a perfectly aligned cavity, for a given ring of sensors at radius r , the mean value of $\Delta P(\phi, r)$ along ϕ is 0 and it has a standard deviation σ_r that comes from scattered light due to the mirrors' roughness and the intrinsic resolution of the sensors. We compute signal to noise ratios $\Delta P(\phi, r)/\sigma_r$ for different values of misalignment and show their distribution in Figure 9. These distributions present a positive peak in the direction of misalignment, and a negative one in the opposite direction, which reflects the fact that the beam is off-centered with respect to the mirror. These characteristic features should be helpful to detect and correct misalignment.

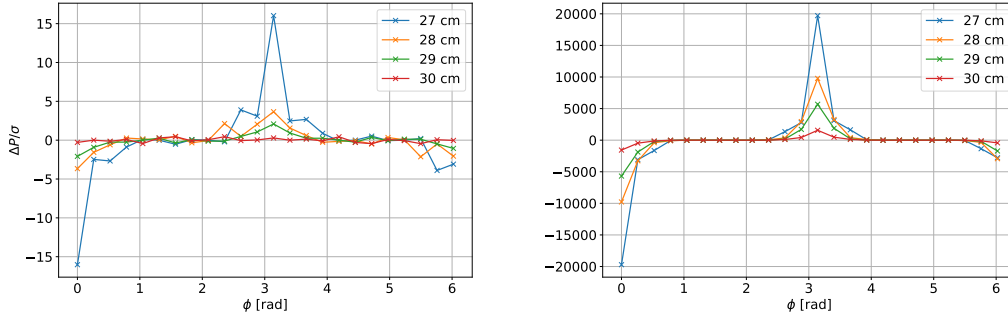


Figure 9. Distribution of the differential power in sensors $\Delta P(\phi, r)/\sigma_r$ as a function of the sensor's angular position ϕ and distance r to the center of the mirror, in the case where the EM is tilted by $3 \cdot 10^{-7}$ rad (left), and $8 \cdot 10^{-7}$ rad (right) along the y axis.

To estimate the range of misalignment that the sensors would be able to monitor, we show in Figure 10 the maximal SNR in a single sensor as a function of the tilt angle. Since sensors closer to the center of the mirror are more sensitive to misalignment, only the 27 cm ring is represented. The excess of power starts to be significant ($\text{SNR} > 5$) just above $0.2 \mu\text{rad}$, and increases exponentially with the angle until $0.6 \mu\text{rad}$. The range $0.2 - 0.6 \mu\text{rad}$ corresponds to the power in the cavity decreasing from 95% to 50% of the power in the perfectly aligned configuration.

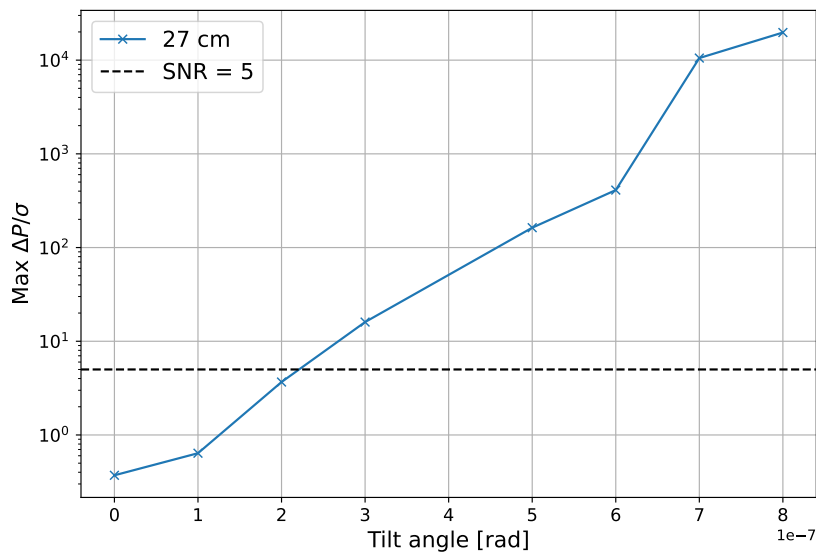


Figure 10. Maximal value of the SNR $\Delta P(\phi, r)/\sigma_r$ for the 27 cm ring as a function of the tilt angle applied to the EM. The black dashed line represents an SNR of 5.

3.3. Point absorbers

Point absorbers (PA) are small, typically around 0.1 mm, highly absorbing areas located on the surface of the mirrors, that generate non-uniform absorption. Several of them have been detected in Virgo and the two LIGO detectors during O3 [9, 10]. These PAs are harmful to the sensitivity of the detector, as they scatter power from the fundamental resonating mode of the beam into higher order modes, decreasing the overall circulating power. In order to detect these defects, one needs to physically inspect the mirrors, which is impractical, and cannot be done during observing runs. That is why we are interested in assessing the ability of instrumented baffles to monitor them.

A PA is simulated in SIS by adding a local surface deformation in the mirror map. It is characterized by its location on the mirror and its total absorbing power. During O3, PAs have been found at distances between 0.1 and 5.4 cm from the center of the mirrors, and their absorbing power estimated around 10 mW [10]. For this reason, we set an absorbing power of 10 mW for the PAs studied here.

Figure 11 shows the radial distribution of power on the EM baffle when a 10 mW PA is placed at the center of EM, and the IM, respectively. In both cases, an excess of power is present as compared to the nominal configuration. When the PA is located on the IM, the surface power is globally constant from 26 to 30 cm, and more than 10 times higher than in the absence of a PA. When a PA is placed on the center of the EM, surface power tends to increase with the radius, reaching a plateau at 29-30 cm. The corresponding power seen by each sensor is shown in Figure 12. Hence, the signature of a PA would be clearly visible as an excess of power in sensors in the first four rings. Contrary to the case of a misalignment, the power does not decrease with radius. Besides, the fact that PAs could be present on both the EM and IM motivates the instrumentation of the baffles around the IM as well.

To study the case where a PA is away from the center of the mirror, we place a 50 mW PA at 5 cm to the right of the center of the EM. The resulting surface power distribution and power in sensors are shown in Figure 13. As for the centered PA, there is a global excess of power in all rings that indicates the presence of a PA. The angular distribution of power is not isotropic due to the presence of Airy rings centered at the position of the PA. Nevertheless, the coverage provided by the sensors is not sufficient to confidently infer the precise position of the PA.

Finally, Table 3 presents the maximal values of power reaching an individual sensor in each ring and for every configuration. A Laser Induced Damage Threshold test has been performed to check the resistance of the sensors to high laser power. It has shown that for a surface power up to 50 W/cm^2 , sensors saturate but are not damaged.

4. Conclusion

The optical simulations presented here are intended to estimate the amount of light that will be seen by sensors installed on the EM baffle in different configurations, in order to

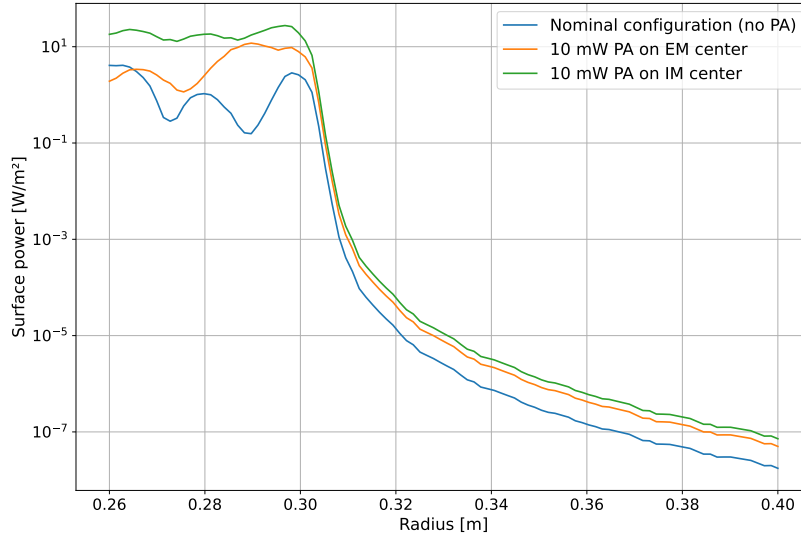


Figure 11. Radial distribution of power on the EM baffle when a 10 mW PA is placed at the center of the EM (orange), and the IM (green). The nominal case where no PA is added is represented in blue.

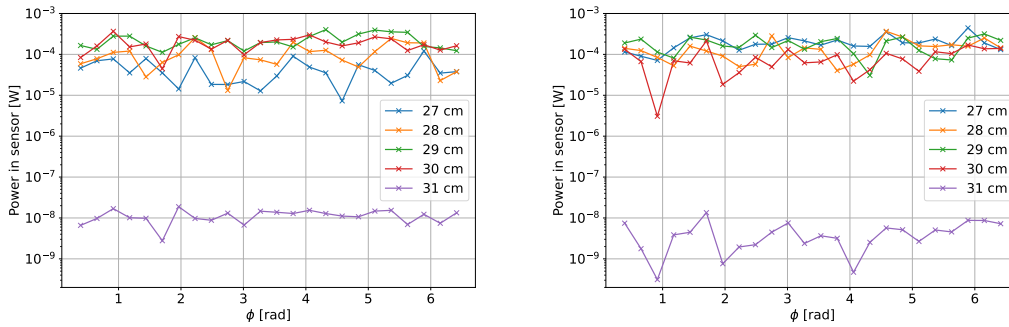


Figure 12. Power seen by each sensor when a PA is placed at the center of the IM (left), and the EM (right). Each color represents a different ring of sensors.

Radius [cm]	Maximal power in one sensor [W]			
	Nominal	0.3 μ rad tilt	0.8 μ rad tilt	10 mW point absorber
27	$4.7 \cdot 10^{-5}$	$2.1 \cdot 10^{-3}$	2.6	$1.8 \cdot 10^{-4}$
28	$1.3 \cdot 10^{-4}$	$6.0 \cdot 10^{-4}$	1.4	$3.2 \cdot 10^{-4}$
29	$1.7 \cdot 10^{-4}$	$4.0 \cdot 10^{-4}$	$7.3 \cdot 10^{-1}$	$6.5 \cdot 10^{-4}$
30	$8.0 \cdot 10^{-5}$	$1.9 \cdot 10^{-4}$	$2.0 \cdot 10^{-1}$	$4.2 \cdot 10^{-4}$
31	$3.8 \cdot 10^{-9}$	$5.2 \cdot 10^{-7}$	$7.1 \cdot 10^{-5}$	$2.5 \cdot 10^{-8}$

Table 3. Maximal power seen by a single sensor in each ring for different configurations.

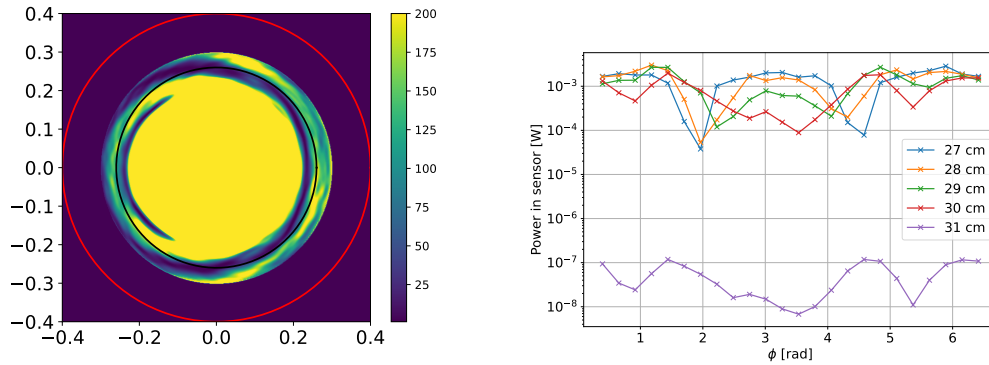


Figure 13. Surface power distribution on the EM and baffle (left) and distribution of power in sensors (right) when a 50 mW PA is placed at 5 cm to the right of the center of the EM.

provide constraints on the sensitivity and dynamic range of sensors, and to demonstrate the ability of this instrument to detect defects in the cavity.

We have shown that the sensors will receive an order of magnitude of 10^{-4} W in nominal conditions when the circulating power in the cavity is 380 kW, with a variability of approximately 100% due to the non-isotropic scattering from the mirrors' surface. Sensors will be able to detect the anti-symmetric difference of power due to a misalignment of the cavity when the deviation of the beam is larger than $0.2 \mu\text{rad}$. This should prove particularly helpful for pre-alignment operations. Sensors will also provide meaningful information about the presence of defects on the mirrors' surface. Simulations show that sensors can confidently detect the signature of a 10 mW PA near the center of the EM or the IM. While inferring the precise number and positions of PAs remains a difficult goal to achieve, instrumented baffles will allow to monitor potential degradation of the mirrors in real time.

Acknowledgments — The authors gratefully acknowledge the European Gravitational Observatory (EGO) and the Virgo Collaboration for providing access to the facilities. The LIGO Observatories were constructed by the California Institute of Technology and Massachusetts Institute of Technology with funding from the National Science Foundation under cooperative agreement PHY-9210038. The LIGO Laboratory operates under cooperative agreement PHY-1764464. This project has received funding from the European Union's Horizon 2020 research and innovation programme under the Marie Skłodowska-Curie grant agreement No. 754510. This work is partially supported by the Spanish MCIN/AEI/10.13039/501100011033 under the Grants No. SEV-2016-0588, No. PGC2018-101858-B-I00, and No. PID2020-113701GB-I00, some of which include ERDF funds from the European Union, and by the MICINN with funding from the European Union NextGenerationEU (PRTR-C17.I1) and by the Generalitat de Catalunya. IFAE is partially funded by the CERCA program of the Generalitat de Catalunya. MAC is supported by the 2022 FI-00335 grant.

References

- [1] Raffaele Flaminio. Status and plans of the Virgo gravitational wave detector. In Heather K. Marshall, Jason Spyromilio, and Tomonori Usuda, editors, Ground-based and Airborne Telescopes VIII, volume 11445, page 1144511. International Society for Optics and Photonics, SPIE, 2020.
- [2] O Ballester, O Blanch, L Cardiel, M Cavalli-Sforza, A Chiummo, C García, J M Illa, C Karathanasis, M Kolstein, M Martínez, A Menéndez-Vázquez, Ll M Mir, J Mundet, A Romero-Rodríguez, D Serrano, and H Yamamoto. Measurement of the stray light in the advanced virgo input mode cleaner cavity using an instrumented baffle. Classical and Quantum Gravity, 39(11):115011, may 2022.
- [3] A. Romero-Rodríguez, A. Allocca, A. Chiummo, M. Martínez, Ll M. Mir, and H. Yamamoto. Determination of the light exposure on the photodiodes of a new instrumented baffle for the Virgo input mode cleaner end-mirror. Classical and Quantum Gravity, 38(4):045002, February 2021.
- [4] M. Andres-Carcasona, O. Ballester, O. Blanch, J. Campos, G. Caneva, L. Cardiel, M. Cavalli-Sforza, P. Chiggiato, A. Chiummo, J. A. Ferreira, J. M. Illa, C. Karathanasis, M. Kolstein, M. Martinez, A. Macquet, A. Menendez-Vazquez, Ll. M. Mir, J. Mundet, A. Pasqualetti, O. Piccinni, C. Pio, A. Romero-Rodriguez, D. Serrano, and V. Dattilo. An instrumented baffle for the Advanced Virgo Input Mode Cleaner End Mirror. arXiv e-prints, page arXiv:2210.16313, October 2022.
- [5] H. Yamamoto, A. Romero, and D. Eto. SIS: Stationary Interferometer Simulation. LIGO laboratory, California Institute of Technology (CalTech), Pasadena, CA, United States of America, 2021. LIGO-T2000311-v2, <https://dcc.ligo.org/LIGO-T2000311/public>.
- [6] Jérôme Degallaix, Christophe Michel, Benoît Sassolas, Annalisa Allocca, Gianpietro Cagnoli, Laurent Balzarini, Vincent Dolique, Raffaele Flaminio, Danièle Forest, Massimo Granata, Bernard Lagrange, Nicolas Straniero, Julien Teillon, and Laurent Pinard. Large and extremely low loss: the unique challenges of gravitational wave mirrors. Journal of the Optical Society of America. A Optics, Image Science, and Vision, 36(11):C85, 2019.
- [7] Raffaele Flaminio. Status and plans of the Virgo gravitational wave detector. In Society of Photo-Optical Instrumentation Engineers (SPIE) Conference Series, volume 11445 of Society of Photo-Optical Instrumentation Engineers (SPIE) Conference Series, page 1144511, December 2020.
- [8] F. Barone, E. Calloni, L. Di Fiore, A. Grado, P. Hello, L. Milano, and G. Russo. Effects of misalignments and beam jitters in interferometric gravitational wave detectors. Physics Letters A, 217(2):90–96, February 1996.
- [9] Aidan F. Brooks et al. Point absorbers in advanced ligo. Applied Optics, 60(13):4047, May 2021.
- [10] M. Cifaldi, E. Cesarini, V. Fafone, M. Lorenzini, D. Lumaca, Y. Minenkov, I. Nardecchia, A. Rocchi, and C. Taranto. Coping with anomalous power absorptions in the Advanced Virgo core optics. Nuovo Cim. C, 45(5):140, 2022.